



Geophysical Research Letters

RESEARCH LETTER

10.1029/2021GL094189

Key Points:

- Linear response function reveals the most excitable mode of September Arctic sea ice, which is maximized over the Pacific side of the Arctic
- Precipitation anomaly over the western and central tropical Pacific ocean and its resulting teleconnection is likely the cause
- Good agreement is found with statistical leading mode of a pre-industrial run, indicating the robustness of linear response function results

Supporting Information:

Supporting Information may be found in the online version of this article.

Correspondence to:

Y. Wu, yutianwu@ldeo.columbia.edu

Citation:

Wu, Y., Lu, J., Ding, Q., & Liu, F. (2021). Linear response function reveals the most effective remote forcing in causing september Arctic Sea ice melting in CESM. *Geophysical Research Letters*, 48, e2021GL094189. https://doi.org/10.1029/2021GL094189

Received 4 MAY 2021 Accepted 24 JUL 2021

Linear Response Function Reveals the Most Effective Remote Forcing in Causing September Arctic Sea Ice Melting in CESM

Yutian Wu¹, Jian Lu², Qinghua Ding³, and Fukai Liu⁴

¹Lamont-Doherty Earth Observatory of Columbia University, Palisades, NY, USA, ²Pacific Northwest National Laboratory, Richland, WA, USA, ³Department of Geography, and Earth Research Institute, University of California, Santa Barbara, Santa Barbara, CA, USA, ⁴Ocean University of China and Qingdao National Laboratory for Marine Science and Technology, Qingdao, China

Abstract We apply the linear response function to investigate the most excitable mode of the September Arctic sea ice in the Community Earth System Model. We find that this sea ice mode preferentially takes place over the Pacific side of the Arctic and its remote forcing corresponds to a dipole pattern of precipitation anomaly in the tropics with an increase of precipitation over the western and central tropical Pacific ocean while a decrease over the Maritime Continent. The tropical precipitation anomaly likely drives a Rossby wave train propagating toward the higher latitudes and leads to a ridge anomaly over the Pacific side of the Arctic, resulting in poleward atmospheric heat transport, enhanced downward longwave radiation and thus melting of the sea ice. In addition, a good agreement is found with the leading tropical-Arctic teleconnection mode in a pre-industrial simulation, supporting the usefulness and robustness of the linear response function method.

Plain Language Summary The minimum state of Arctic sea ice in September has experienced a drastic decline in the past two decades and is projected to continue to decline in the future warming climate. It is of both scientific and societal importance to understand both the year-to-year variability and anthropogenic change of the Arctic sea ice and their underlying physical mechanisms. This study, via a novel dynamical approach rather than a statistical one, reveals the optimal forcing pattern that excites the largest sea ice response in September. Our results will contribute to an improved understanding of both the natural variability and anthropogenic change of the September Arctic sea ice in climate model simulations.

1. Introduction

The Arctic sea ice reaches its minimum state during boreal summer and fall and is also the most susceptible to climate forcing during these seasons (e.g., Devasthale et al., 2013; Stroeve et al., 2012). Therefore, it is of both scientific and societal importance to understand the predictability of the Arctic sea ice during summer and fall seasons and its underlying physical mechanism. Several factors are found to affect the predictability skill of the September Arctic sea ice on interannual time scales including the initial states of sea ice, oceans and stratosphere in and around the Arctic in the pre-melting seasons (e.g., preceding winter and spring) (see a review paper by Guemas et al., 2014 and references therein) and atmospheric teleconnection in summer (Baxter et al., 2019; Ding et al., 2014, 2019). For example, Baxter et al. (2019) found a leading tropical-Arctic teleconnection during 1979-2017 summers in observations and showed that sea surface temperature (SST) cooling over the eastern central tropical Pacific ocean and resulting decreased convection likely drives a Rossby wave train toward the Arctic and results in an anomalous high pressure over northeastern Canada and Greenland that in turn plays a key role in melting the sea ice in the region. They also argued that this "Pacific-Arctic (PARC) teleconnection" pattern was responsible for the observed accelerated Arctic sea ice melting from 2007 to 2012. However, Baxter et al. (2019) also noted that a 1800-year long pre-industrial simulation of the Community Earth System Model version 1 (CESM1) can't replicate the observed PARC teleconnection and instead simulates a leading coupled pattern that links a warm western and central tropical Pacific SST to an anomalous high pressure over the Pacific side of the Arctic. The discrepancy between observations and models is not entirely clear and could possibly be due to either model limitations and/or

© 2021. American Geophysical Union. All Rights Reserved.

WU ET AL. 1 of 9



a strong contribution of internal variability in the generation of the PARC. A recent study of Bonan and Blanchard-Wrigglesworth (2020) cautioned the stationarity of the observed PARC pattern because of the short observational record and showed that climate models are able to simulate the observed PARC pattern in decadal timescale but not over longer, centennial timescales.

To make progress, there are two possible approaches to help us better understand the sensitivity of September sea ice to remote forcing, including either using longer proxy records in the past centuries and millennia to explore the stability of the PARC or examining how sea ice in climate models preferentially responds to forcing originating outside the Arctic. In this study, we use a modeling approach and investigate two key questions: (a) what is the most excitable mode of the September Arctic sea ice and (b) what is the corresponding most effective remote atmospheric/oceanic forcing in driving this mode of sea ice? A physical understanding of the above two questions would help better understand and interpret both the natural variability and anthropogenic change of the September Arctic sea ice in climate model simulations. To address the questions, we will make use of a set of q-flux Green's function perturbation experiments and construct the linear response function that explicitly and causally links the Arctic sea ice concentration response to ocean q-flux forcing. To be discussed later, the linear response function approach is useful in identifying a causal relationship between the forcing and response, as compared to conventional statistical methods.

2. Methods and Data

2.1. Linear Response Function

The linear response function (LRF) has proved to be a powerful way for establishing the fundamental forcing-response relationship. A dynamical climate system can be formulated as (Palmer, 1999):

$$\dot{\mathbf{x}} = \mathbf{L}\mathbf{x} + \mathbf{A}\mathbf{f},\tag{1}$$

where x denotes the response in state variables in the climate system, f represents the external forcing, L is the LRF that represents the dynamical climate system response to the forcing and is a square matrix, and A works to bridge the forcing to the response and could be a non-square matrix if the forcing and response are different variables and have different spatial coverage. Since we focus on the equilibrium response, $\dot{x}=0$ and Equation 1 can be written as

$$\mathbf{A}^{-1}\mathbf{L} = -\mathbf{f} \times \mathbf{x}^{-1}.\tag{2}$$

We define $\tilde{\mathbf{L}} = \mathbf{A}^{-1}L$ and $\tilde{\mathbf{L}}$ plays a similar role as the LRF \mathbf{L} as in the literature. There are different ways one can construct $\tilde{\mathbf{L}}$. Here we adopt the Green's function approach built on a set of forced model experiments (to be discussed next) as it is found to be more effective and accurate in reproducing the modeled response (F. Liu, Lu, Garuba, Leung, et al., 2018), despite the computational cost of the experiments. Once $\tilde{\mathbf{L}}$ is constructed from the model experiments following Equation 2, its singular vectors can be used to identify the most excitable mode of the response, which exhibits the largest response to forcing and is known as the neutral vector, and its most effective forcing (Barsugli & Sardeshmukh, 2002; Goodman & Marshall, 2002; Hassanzadeh & Kuang, 2016; Marshall & Molteni, 1993; F. Liu, Lu, Garuba, Harrop, et al., 2018; Dong et al., 2019; F. Liu, Lu, Garuba, Leung, et al., 2018; Lu et al., 2020). The neutral vector is the right singular vector of $\tilde{\mathbf{L}}$ associated with the smallest singular number (see detailed discussions in Goodman & Marshall, 2002) and the optimal forcing needed to produce the neutral vector is the left singular vector. For example, Hassanzadeh and Kuang (2016) examined the LRF and neutral vector in a dry dynamical core and found that the neutral vector is the annular mode pattern, as such assigning dynamical attribute to the annular mode, which is often derived from statistical analysis.

2.2. Model Experiments

To construct the LRF that links remote atmospheric/oceanic forcing to Arctic sea ice response, we will make use of a set of q-flux perturbation experiments by F. Liu, Lu, Garuba, Leung, et al. (2018). The experiments are performed by using the slab ocean model (SOM) configuration of the CESM1.1 (Hurrell et al., 2013) which includes the Community Atmosphere Model version 5 (CAM5) (2.5° longitude by 1.9° latitude horizontal resolution) and a thermodynamic sea ice component of the Community Ice Code (CICE).

WU ET AL. 2 of 9

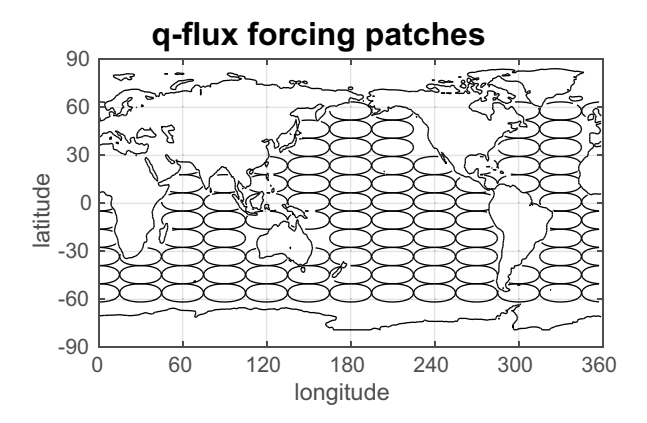


Figure 1. Configuration of q-flux perturbation patches following Equation 3. Each ellipse indicates 6 W/m² contour. Note that the actual size of the patch is larger than the contoured area and the adjacent patches overlap.

The control simulation is a 900-year long CESM1.1-SOM forced with pre-industrial carbon dioxide levels and solar radiation and specified climatological ocean mixed layer depth h and ocean heat transport q-flux. The SST is prognostic and calculated based on the thermal coupling between the SOM and the atmosphere. For the perturbation experiments, 97 pairs of localized "warm patch" and "cold patch" simulations are performed, in which an anomalous q-flux patch is added to or subtracted from the climatological q-flux. Each q-flux patch anomaly is specified as the following

$$Q\cos^{2}\left(\frac{\pi}{2}\frac{\lambda-\lambda_{k}}{\lambda_{w}}\right)\cos^{2}\left(\frac{\pi}{2}\frac{\phi-\phi_{k}}{\phi_{w}}\right)$$
 (3)

Within the rectangular patch ($\lambda_k \pm \lambda_w$, $\phi_k \pm \phi_w$), and zero elsewhere. $Q = \pm 12 \text{ W/m}^2$ is the amplitude of the q-flux anomaly, $\lambda_w = 30^\circ$ longitude, $\phi_w = 12^\circ$ latitude, and (λ_k , ϕ_k) is the atmospheric grid that lies over the ocean with λ_k from 0°E to 330°E with an interval of 30° and ϕ_k from 67.26°S to 57.79°N with an interval of 11.37°. The q-flux perturbation patches are shown in Figure 1. While the computational cost requires a trade-off between model complexity and number of perturbation exper-

iments, we note the possible limitation of using a thermodynamic sea ice model in fully capturing the sea ice variability. Each q-flux patch perturbation experiment is integrated for 40 years and the average of the last 20 years of equilibrium response is used for analysis. In this study, we examine the linear component of the response by estimating $(\mathbf{x}_+ - \mathbf{x}_-) / 2$ with subscripts + and – denoting the positive and negative forcing experiments, respectively, as the linear component approximates the actual response when the forcing is small (Gritsun, 2010).

It's worth emphasizing that the LRF method, aided by the design of Green's function-type forcing perturbations, is rooted in dynamics rather than statistics and helps to establish a causal relationship between the forcing and response. Although many existing studies have focused on identifying lagged correlation and regression relationships between the atmospheric circulation and Arctic sea ice (e.g., Baxter et al., 2019; Bonan & Blanchard-Wrigglesworth, 2020), lagged correlation or regression alone can not indicate the direction of causality because the relationship can be biased by autocorrelation, common drivers (so no direct links between the two processes), or indirect links via a third process, which are common in climate science (e.g., Kretschmer et al., 2016; Runge et al., 2019). Instead forcing is explicit in q-flux perturbation experiments and the cause-and-effect relationship can be established using these experiments and the LRF method.

We use the LRF method and q-flux model experiments to explore the most excitable mode of the September Arctic sea ice and the optimal forcing that excites the mode. First, we construct L following Equation 2. f is the q-flux perturbation forcing and has $M \times J$ dimension with M representing the number of grid points over the ocean covered by q-flux perturbation patches and J representing the number of perturbation experiments. x is the linear component of the September Arctic sea ice concentration response and has a dimension of $N \times J$ with N indicating the number of grid points covering the Northern Hemisphere sea ice area. And thus $\tilde{\mathbf{L}}$ has $M \times N$ dimension, independent of the number of experiments. Since \mathbf{x} is not necessarily a square matrix, we calculate \mathbf{x}^{-1} using pseudo-inversion as $(\mathbf{x}^{T} \times \mathbf{x})^{-1} \times \mathbf{x}^{T}$, where superscript \mathbf{T} denotes transpose, and $\mathbf{x}^T \times \mathbf{x}$ is found to be well-conditioned and invertible in our study. Then we calculate the neutral vector as the right singular vector of L associated with the smallest singular number and thus maximum response-to-forcing ratio, which reveals the most excitable mode of the September Arctic sea ice. We note that the smallest and 2nd smallest singular values are statistically distinguishable at the 95% confidence level based on Jackknife resampling method (not shown). The optimal forcing, which is calculated as the left singular vector, indicates the associated most effective q-flux forcing in driving the September Arctic sea ice mode. The other variables (**Z**, such as sea level pressure and precipitation) associated with the neutral vector and optimal forcing can be estimated as $\mathbf{Z}_n \approx \mathbf{Z}\mathbf{f}^{-1}\mathbf{f}_n$ with subscript *n* denoting mode number.

WU ET AL. 3 of 9

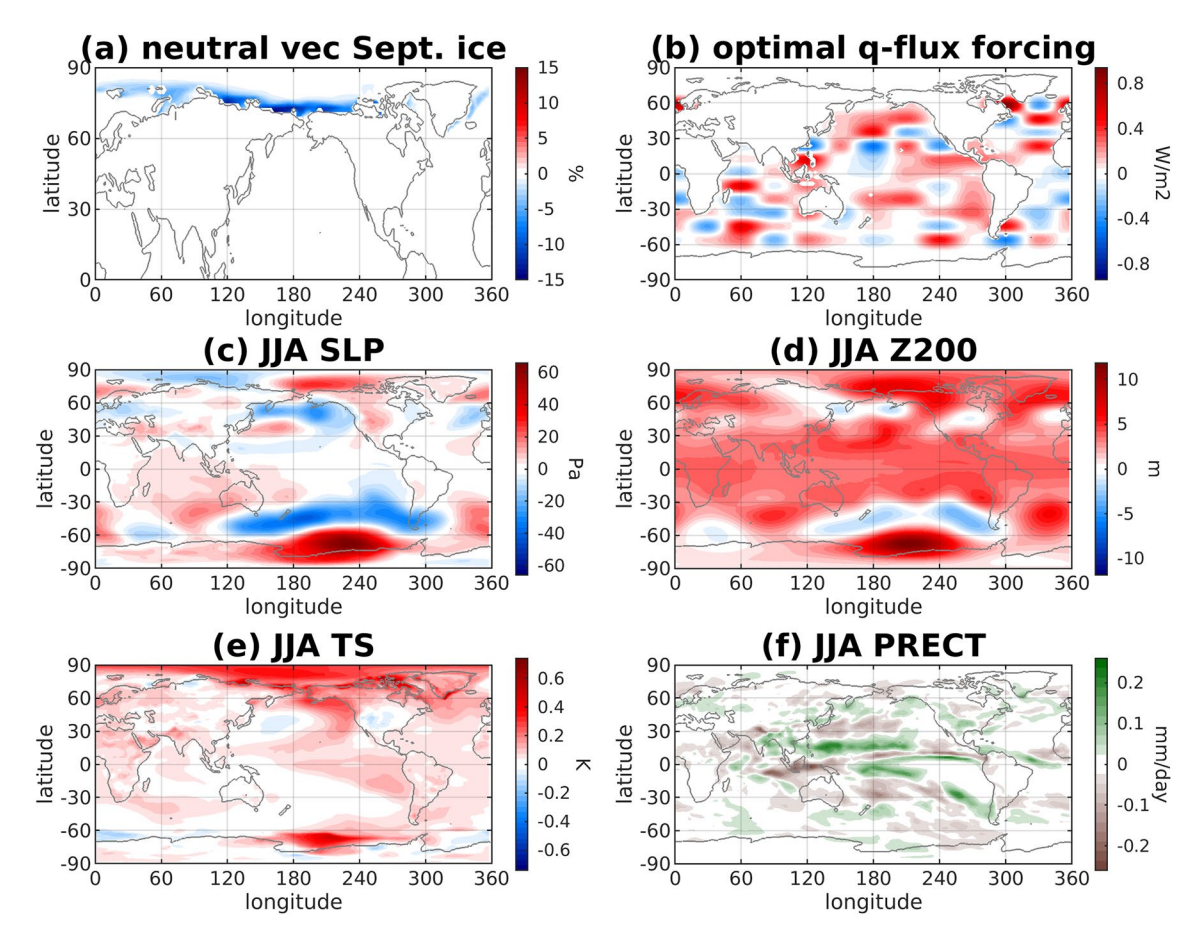


Figure 2. (a) The neutral vector for September Arctic sea ice and (b) its corresponding optimal *q*-flux forcing. The associated June-July-August (c) sea level pressure, (d) 200 hPa geopotential height (Z200), (e) surface temperature (TS), and (f) precipitation (PRECT) with the neutral vector. The neutral vector is scaled so that the maximum sea ice loss is 15%. The optimal forcing is scaled by the smallest singular number and also the neutral vector rescaling.

3. Results

Figures 2a and 2b shows the neutral vector for September Arctic sea ice and the corresponding optimal q-flux forcing. The neutral vector shows that the largest sea ice decrease occurs primarily over the Pacific side of the Arctic, that is, the Beaufort Sea, the East Siberia Sea and the Laptev Sea. The corresponding optimal q-flux forcing shows complex patchy areas of positive and negative values in the globe, and the patchiness is due to the experimental design with a limited number of q-flux patches covering the global ocean (Figure 1). While positive q-flux anomalies are primarily seen over the central and eastern tropical Pacific ocean, the South China Sea, the Philippine Sea, the midlatitude North Pacific ocean, the Labrador Sea and other places, negative q-flux anomalies are found over the East China Sea, the subtropical North Pacific ocean and others, both acting to drive an overall decrease of the Arctic sea ice in September. As guided by the LRF approach, if we were to perform a model experiment by prescribing the optimal q-flux forcing pattern as in Figure 2b and ensuring a very small forcing magnitude so that linearity holds, we would expect to obtain a September Arctic sea ice melting pattern as revealed by the neutral vector in Figure 2a. However, additional model experiments and sensitivity tests would be needed to confirm this forcing-response relationship. The optimal q-flux forcing result is also found to be similar in a simple composite analysis based on experiments that correspond to a large decline of September Arctic sea ice (not shown).

Because of the coupling of the SOM and atmospheric model, imposed q-flux perturbations outside of the Arctic region do not cause Arctic sea ice changes directly but instead lead to changes in SST outside of the Arctic region and further changes in precipitation and atmospheric teleconnection, which melts the Arctic sea ice. It's thus helpful to show the associated atmospheric fields, including sea level pressure, 200 hPa geopotential height, surface temperature and precipitation (Figures 2c-2f), to better reveal the linkage

WU ET AL. 4 of 9



between the neutral vector and optimal forcing. Considering the lead-lag relationship between the atmospheric fields and September Arctic sea ice, we use June-July-August (JJA) averaged atmospheric fields following previous studies due to their strong correlation (e.g., Bonan & Blanchard-Wrigglesworth, 2020; Ding et al., 2019). Both the sea level pressure and 200 hPa geopotential height show a wave train-like pattern over the North Pacific ocean toward the Arctic with a positive geopotential height anomaly over the subtropical North Pacific as well as the East Siberia Sea, the Beaufort Sea, and northwestern Canada while a negative anomaly over the mid-to-high latitude North Pacific ocean. Interesting wave train patterns are also found over the Southern Hemisphere, however, they are beyond the scope of this study. For surface temperature and precipitation over the ocean, a positive q-flux anomaly is typically associated with a local increase of surface temperature and precipitation, for example, over the South China Sea and the Philippine Sea (this can be seen in Figure S2 that shows the response in the experiment where a positive q-flux anomaly is imposed around 120°E 12°N). However, remote changes in surface temperature and precipitation can also be generated (for example, a ridge anomaly and a warming anomaly can be seen over the Pacific side of the Arctic in Figure S2). In Figure 2e, in addition to a warming pattern over the Pacific side of the Arctic, warming is also seen over the central and eastern tropical Pacific ocean and eastern North Pacific ocean while cooling is found over the western North Pacific ocean, which resembles the positive phase of the Interdecadal Pacific Oscillation (IPO). Screen and Deser (2019) found a very similar atmospheric teleconnection toward the Arctic following the positive IPO phase and argued a faster Arctic sea ice loss during the positive IPO phase compared to the negative IPO phase. For precipitation (Figure 2f), interesting patterns are found at lower latitudes, including an increased precipitation over the Philippine Sea extending to central subtropical North Pacific ocean as well as the western and central tropical Pacific ocean while a decreased precipitation primarily over the Maritime Continent. In terms of the magnitude, overall we find that a tropical warming of about 0.1-0.2 K and a tropical precipitation increase of about 0.1-0.2 mm/day are linked to a sea ice melting as large as 10%-15% over the Arctic. These numbers are in good agreement with the composited extreme sea ice loss results found in Baxter et al. (2019) (see their Figures 11 and 12) despite of the different methodology and use of full ocean and sea ice models therein.

To confirm the accuracy of the calculated neutral vector and optimal forcing, we also compute them using the sensitivity matrix approach, which doesn't involve matrix inversion (see details in Supporting Information). It's found that the results using the sensitivity matrix approach (Figure S1) are largely consistent with those using the LRF. The neutral vector shows a similar maximal sea ice loss over the Pacific side of the Arctic although large sea ice loss is also found over the Kara Sea in the sensitivity matrix approach (Figure S1a). Similarity is also found in the optimal q-flux forcing (Figure S1b) except that the q-flux forcing is slightly smoother in its spatial pattern and has a slightly larger amplitude in the sensitivity matrix approach compared to the LRF approach. The associated atmospheric fields also resemble between the two approaches (Figure S1c–S1f), supporting the robustness of the LRF results.

The importance of the positive geopotential height anomaly over the Pacific side of the Arctic has also been emphasized in previous observational and modeling studies (e.g., L'Heureux et al., 2008; Baxter et al., 2019; Screen and Deser, 2019). For example, L'Heureux et al. (2008) attributed the drastic sea ice loss over the western Arctic during 2007 summer to an unusually high Pacific-North American (PNA) index and an associated strong anticyclone anomaly in this region, which is very similar to our geopotential height anomaly (see their Figure 2a). Similarly, a recent study of Z. Liu et al. (2021) also linked the variability and trend of western Arctic sea ice during late summer to the PNA pattern. In our case, the high pressure anomaly over the Pacific side of the Arctic drives an anomalous poleward heat transport in the region (Figure 3a). This leads to a warming of the Arctic atmospheric column (Figure 3b) and an enhanced downward longwave radiation at the surface (Figure 3c), particularly over the Laptev Sea and East Siberian Sea, leading to the melting of the sea ice. The linkage between the meridional heat transport and atmospheric warming is, however, less clear over the Atlantic side of the Arctic, but the sea ice melting is smaller anyway (Figure 2a). Figure 3d shows a reduction of the upward solar radiation at the surface, likely due to the sea ice melting, reflecting a positive ice albedo feedback.

Therefore, the LRF and q-flux perturbation experiments reveal the most excitable mode of the September Arctic sea ice, which is maximized over the Pacific side of the Arctic. The associated most effective q-flux forcing is complex in its spatial pattern and its corresponding precipitation shows a dominant dipole pattern

WU ET AL. 5 of 9

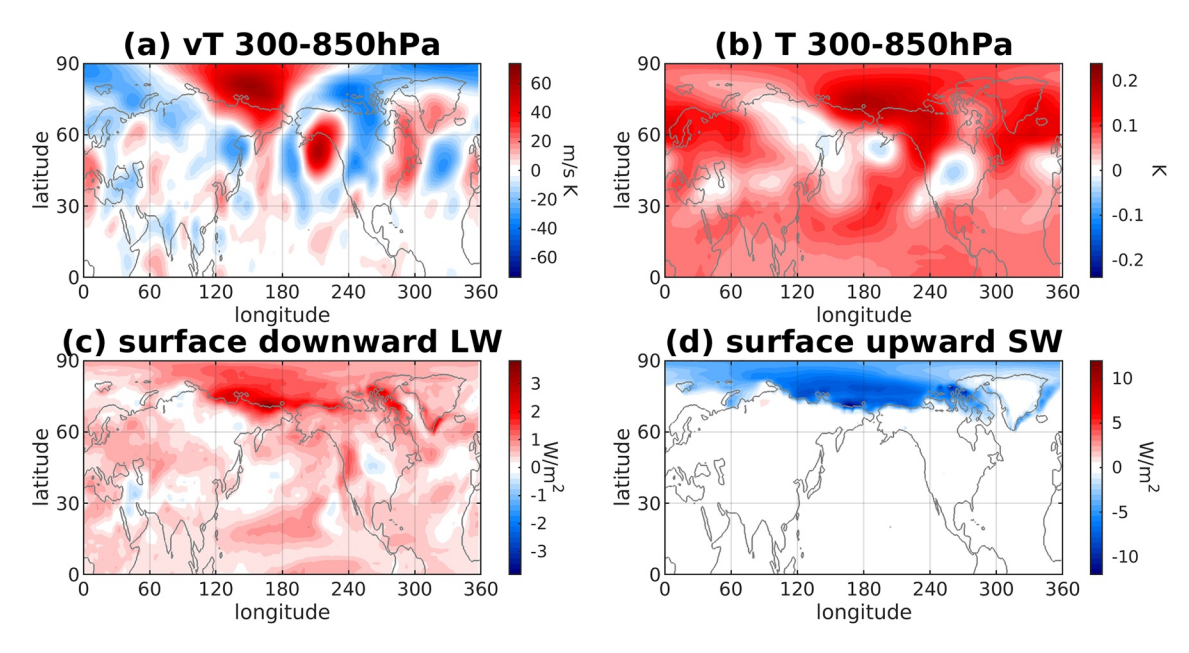


Figure 3. The associated June-July-August (a) 300–850 hPa averaged total meridional heat flux, (b) 300–850 hPa averaged temperature, (c) surface downward longwave (LW) radiation, and (d) surface upward shortwave (SW) radiation with the neutral vector.

in the tropics with an increased precipitation over the western and central tropical Pacific and a decreased precipitation over the Maritime Continent. The tropical precipitation pattern likely drives a Rossby wave train propagating toward higher latitudes, resulting in a trough over high latitude North Pacific ocean and a ridge over the Pacific side of the Arctic extending to northwestern Canada. We find our wave train response in the tropical to midlatitude western Pacific region similar to the Pacific-Japan pattern, in which the summertime anticyclonic anomalies over the midlatitude Far East is linked to enhanced convective activity near the Philippines and its resulting teleconnection pattern (e.g., Kosaka & Nakamura, 2006, 2010; Nitta, 1987; Tsuyuki & Kurihara, 1989). However, since most of the Pacific-Japan pattern studies focus on the tropical to midlatitude region, its influence on the Arctic is not clear.

Finally we show that the neutral vector, which is constructed based on dynamics, is, in fact, in good agreement with the statistical leading pattern of September Arctic sea ice identified from the Maximum Covariance Analysis (MCA). To recapitulate, MCA isolates pairs of spatial patterns and corresponding time series by performing the eigenanalysis on the temporal covariance matrix between two space-time varying variables, and MCA mode 1 explains the maximum fraction of the covariance that is, obtained from the leading mode of the singular value decomposition of the covariance matrix. Figure 4 shows the MCA mode 1 between the September Arctic sea ice and JJA tropical SST as well as associated correlation with JJA 200 hPa geopotential height and tropical precipitation calculated from a 1800-year long CESM1 pre-industrial simulation. Since the conventional normalization for MCA left and right singular vectors (i.e., multiplying by the standard deviation of the time series) is different from the normalization for neutral vector, for simplicity, we show the non-normalized results for MCA and compare the MCA and neutral vector results in patterns. The CESM2, which is the latest generation of the coupled climate models developed at NCAR and includes substantial model developments and improvements (Danabasoglu et al., 2020), shows consistent MCA results (Figure S3). Similar to the neutral vector (Figure 2a), the statistical leading mode of September Arctic sea ice (Figure 4a) is maximized over the Pacific side of the Arctic, except that the pattern is slightly shifted westward and extends to the Kara Sea compared to the neutral vector. A similar wave train pattern is also found for 200 hPa geopotential height (Figure 4a) with a positive anomaly over the Northern Hemisphere tropical and subtropical region, a negative anomaly over the North Pacific ocean and a positive anomaly over the Pacific side of the Arctic, except that the midlatitude negative height anomaly spans over a larger area in comparison to the neutral vector results (Figure 2d). In addition, both the tropical SST and precipitation (Figure 4b) resemble the results from the neutral vector (Figures 2e and 2f). In particular, a dipole pattern is found in tropical precipitation with a positive anomaly over the tropical Pacific ocean and the

WU ET AL. 6 of 9

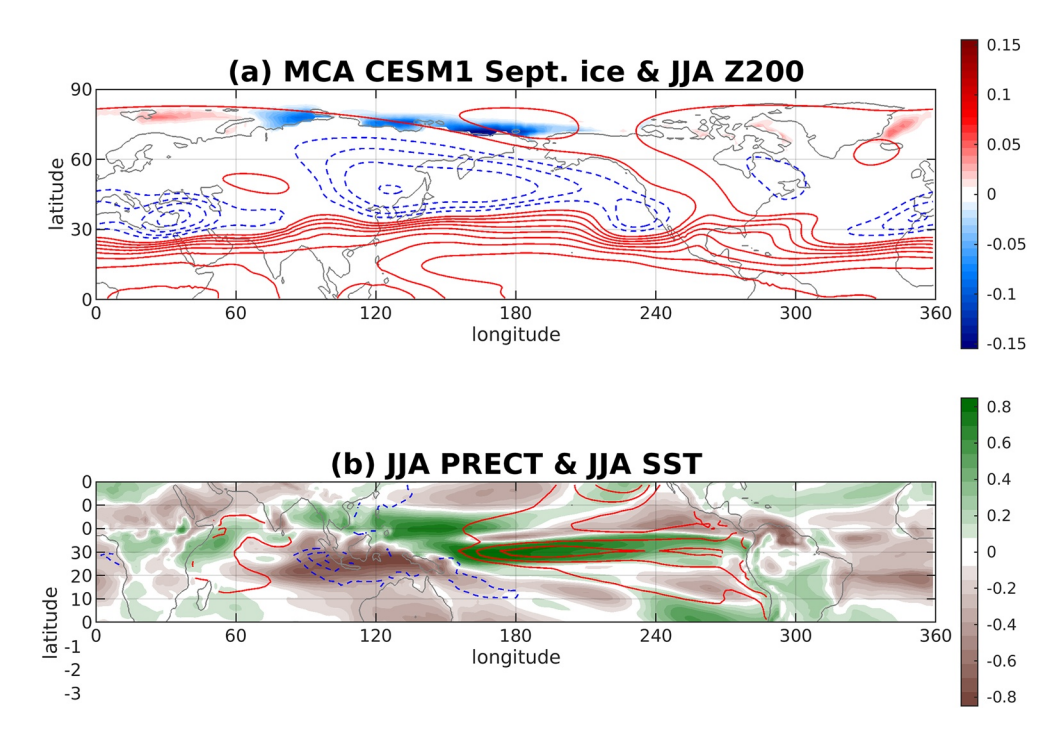


Figure 4. Maximum Covariance Analysis (MCA) mode 1 of September Arctic sea ice and June-July-August (JJA) tropical SST in the 1800-year long CESM1 pre-industrial control simulation. (a) September Arctic sea ice concentration (left singular vector, color shadings, orthogonal and unitless because of SVD analysis) and associated correlation with JJA Z200 (contours with contour interval of 0.1). (b) SST (right singular vector, contours with contour interval of 0.015, orthogonal and unitless because of SVD analysis) and correlation with JJA tropical precipitation (color shadings, unitless). For the result of Z200, it's calculated as the correlation between the time series associated with sea ice mode 1 and the original Z200 data. And similarly for precipitation. Red contours indicate positive values and blue contours indicate negative values.

Philippine Sea and a negative anomaly over the Maritime Continent. In comparison to the neutral vector results, the MCA shows a more dominant precipitation increase over the equatorial Pacific than off-equatorial tropical Pacific west of the Philippine Sea, likely due to the ocean dynamics in fully coupled CESM and dominant oceanic forcing over the equatorial Pacific. In summary, this overall agreement suggests that the statistical leading pattern of summertime atmospheric circulation and September Arctic sea ice indeed reflects the fundamental, dynamical, and more importantly causal relationship between the two.

4. Conclusion and Discussions

In this study, we apply the linear response function to investigate the most excitable mode of the September Arctic sea ice, which preferentially occurs over the Pacific side of the Arctic. The corresponding most effective remote forcing in driving this mode of Arctic sea ice consists of complex patchy areas of positive and negative values of q-flux forcing in the globe. The signs of q-flux forcing indicate that positive q-flux forcing in some regions while negative forcing in others corresponds to an overall melting of the Arctic sea ice. The corresponding atmospheric fields reveal interesting features related to atmospheric teleconnection patterns, including a positive IPO-like SST pattern and an increase of precipitation over the western tropical and subtropical Pacific ocean while a decrease over the Maritime Continent, which drives a Rossby wave train propagating toward the higher latitudes and results in a ridge anomaly over the Pacific side of the Arctic. The resulting poleward atmospheric heat transport and enhanced downward longwave radiation likely lead to the sea ice melting in the region. Furthermore, a good agreement is found between the neutral vector and the statistical leading pattern of the MCA from a long pre-industrial simulation. This agreement not only supports the usefulness and robustness of the linear response function method but also confirms the fundamental, dynamical and causal relationship between summertime atmospheric circulation and September Arctic sea ice in climate models.

WU ET AL. 7 of 9



Our study emphasizes the importance of summertime atmospheric teleconnection in determining the September Arctic sea ice variability in climate models, especially the role of the western and central tropical Pacific. In future projections, although state-of-the-art climate models project a reduced zonal gradient of SST over the equatorial Pacific with rising greenhouse gases (e.g., Coats & Karnauskas, 2017), studies have challenged the model results and argued a strengthening of the tropical Pacific zonal SST gradient based on the fundamental dynamics and thermodynamics of the tropical ocean-atmosphere interaction (Seager et al., 2019). If tropical Pacific zonal SST gradient were indeed to strengthen in the future climate, it would likely result in significant global consequences that would deviate from current climate model projections, including a different rate of Arctic sea ice melting (Screen & Deser, 2019).

Our study reveals the most excitable mode of the September Arctic sea ice and the most effective remote forcing in causing the mode in CESM. This is a mode that is, most likely to be excited and exhibits the largest response to forcing and thus plays an important role in understanding and interpreting both the natural variability and anthropogenic change of the Arctic sea ice. It is noted that in this set of q-flux perturbation experiments, the nonlinear component is found to be comparable to the linear component in magnitude (Lu et al., 2020), and its resulting possible impact on the accuracy of the linear component might deserve further investigation. We also note that the neutral vector and optimal forcing are derived from a single atmospheric general circulation model coupled to a slab ocean model and a thermodynamic sea ice model, so the results could possibly be affected by model biases and it might be worth repeating the exercise with other atmospheric models and coupled to a full ocean and sea ice model as sea ice dynamics are important in driving sea ice variability (Ogi et al., 2010). In addition, future work will extend the analysis to other seasons over the Arctic as well as the Antarctica.

Data Availability Statement

The data produced for and analyzed in this paper are available through Columbia University Academic Commons. https://academiccommons.columbia.edu/doi/10.7916/d8-vpgy-5h91.

Acknowledgments References

Yutian Wu acknowledge the support from NSF OPP-1825858 and the Lamont Center for Climate and Life Fellowship. Jian Lu is supported by the U.S. Department of Energy Office of Science Biological and Environmental Research as part of the Regional and Global Modeling and Analysis Program area. Qinghua Ding is supported by NSF's Polar Programs (OPP-1744598) and Modeling, Analysis, Predictions and Projections (NA19OAR4310281), and Climate Variability and Predictability (NA18OAR4310424) programs as part of NOAA's Climate Program Office. Fukai Liu is supported by the National Natural Science Foundation of China (NSFC; 41906002 and 91858210). We acknowledge the CESM Large Ensemble Community Project and supercomputing resources provided by NSF/CISL/

Yellowstone.

Barsugli, J. J., & Sardeshmukh, P. D. (2002). Global atmospheric sensitivity to tropical SST anomalies throughout the Indo-Pacific basin. Journal of Climate, 15, 3427–3442. https://doi.org/10.1175/1520-0442(2002)015<3427:GASTTS>2.0.CO;2

Baxter, I., Ding, Q., Schweiger, A., L'Heureux, M., Baxter, S., Wang, T., et al. (2019). How tropical pacific surface cooling contributed to accelerated sea ice melt from 2007 to 2012 as ice is thinned by anthropogenic forcing. *Journal of Climate*, 32, 8583–8602. https://doi.org/10.1175/JCLI-D-18-0783.1

Bonan, D. B., & Blanchard-Wrigglesworth, E. (2020). Nonstationary teleconnection between the Pacific ocean and Arctic sea ice. *Geophysical Research Letters*, 47, e2019GL085666. https://doi.org/10.1029/2019GL085666

Coats, S., & Karnauskas, K. B. (2017). Are simulated and observed twentieth century tropical pacific sea surface temperature trends significant relative to internal variability? *Geophysical Research Letters*, 44, 9928–9937. https://doi.org/10.1002/2017GL074622

Danabasoglu, G., Lamarque, J.-F., Bacmeister, J., Bailey, D. A., DuVivier, A. K., Edwards, J., et al. (2020). The Community Earth System Model version 2 (CESM2). *Journal of Advances in Modeling Earth Systems*, 12, e2019MS001916. https://doi.org/10.1029/2019MS001916 Devasthale, A., Sedlar, J., Koenigk, T., & Fetzer, E. J. (2013). The thermodynamic state of the Arctic atmosphere observed by AIRS: Comparisons during the record minimum sea ice extents of 2007 and 2012. *Atmospheric Chemistry and Physics*, 13, 7441–7450. https://doi.org/10.5194/acp-13-7441-2013

Ding, Q., Schweiger, A., L'Heureux, M., Steig, E. J., Battisti, D. S., Johnson, N. C., et al. (2019). Fingerprints of internal drivers of Arctic sea ice loss in observations and model simulations. *Nature Geoscience*, 12, 28–33. https://doi.org/10.1038/s41561-018-0256-8

Ding, Q., Wallace, J. M., Battisti, D. S., Steig, E. J., Gallant, A. J. E., Ki, H. J., & Geng, L. (2014). Tropical forcing of the recent rapid Arctic warming in northeastern Canada and Greenland. *Nature*, 509, 209–212. https://doi.org/10.1038/nature13260

Dong, Y., Proistosescu, C., Armour, K. C., & Battisti, D. S. (2019). Attributing historical and future evolution of radiative feedbacks to regional warming patterns using a Green's function approach: The preeminence of the western Pacific. *Journal of Climate*, 32, 5471–5491. https://doi.org/10.1175/JCLI-D-18-0843.1

Goodman, J. C., & Marshall, J. (2002). Using neutral singular vectors to study low-frequency atmospheric variability. *Journal of the Atmospheric Sciences*, 59, 3206–3222. https://doi.org/10.1175/1520-0469(2002)059<3206:UNSVTS>2.0.CO;2

Gritsun, A. (2010). Construction of the response operators to small external forcings for atmospheric general circulation atmospheric models with time periodic right-hand sides. *Izvestiya-Atmospheric and Oceanic Physics*, 46, 748–756. https://doi.org/10.1134/S000143381006006X

Guemas, V., Blanchard-Wrigglesworth, E., Chevallier, M., Day, J. J., Deque, M., Doblas-Reyes, F. J., et al. (2014). A review on Arctic sea-ice predictability and prediction on seasonal to decadal time-scales. *Quarterly Journal of the Royal Meteorological Society*, 142, 546–561. https://doi.org/10.1002/qj.2401

Hassanzadeh, P., & Kuang, Z. (2016). The linear response function of an idealized atmosphere. Part I: Construction using Green's functions and applications. *Journal of the Atmospheric Sciences*, 73, 3423–3439. https://doi.org/10.1175/JAS-D-15-0338.1

WU ET AL. 8 of 9



- Hurrell, J. W., Holland, M. M., Gent, P. R., Ghan, S., Kay, J. E., Kushner, P. J., et al. (2013). The community earth system model: A framework for collaborative research. *Bulletin of the American Meteorological Society*, 94, 1339–1360. https://doi.org/10.1175/BAMS-D-12-00121.1
- Kosaka, Y., & Nakamura, H. (2006). Structure and dynamics of the summertime Pacific-Japan teleconnection pattern. Quarterly Journal of the Royal Meteorological Society, 132, 2009–2030. https://doi.org/10.1256/qj.05.204
- Kosaka, Y., & Nakamura, H. (2010). Mechanisms of meridional teleconnection observed between a summer monsoon system and a subtropical anticyclone. Part I: The Pacific-Japan pattern. *Journal of Climate*, 23, 5085–5108. https://doi.org/10.1175/2010JCLI3413.1
- Kretschmer, M., Coumou, D., Donges, J. F., & Runge, J. (2016). Using causal effect networks to analyze different Arctic drivers of midlatitude winter circulation. *Journal of Climate*, 29, 4069–4081. https://doi.org/10.1175/JCLI-D-15-0654.1
- L'Heureux, M. L., Kumar, A., Bell, G. D., Halpert, M. S., & Higgins, R. W. (2008). Role of the Pacific-North American (PNA) pattern in the 2007 Arctic sea ice decline. *Geophysical Research Letters*, 35, L20701. https://doi.org/10.1029/2008GL035205
- Liu, F., Lu, J., Garuba, O., Harrop, B., Leung, L. R., Luo, Y., & Luo, Y. (2018). The sensitivity of surface temperature to oceanic forcing via q-flux Green's function experiments. Part II: Feedback decomposition and polar amplification. *Journal of Climate*, 31, 6745–6761. https://doi.org/10.1175/JCLI-D-18-0042.1
- Liu, F., Lu, J., Garuba, O., Leung, L. R., Luo, Y., & Wan, X. (2018). The sensitivity of surface temperature to oceanic forcing via q-flux Green's function experiments. Part I: Linear response function. *Journal of Climate*, 31, 3625–3641. https://doi.org/10.1175/JCLI-D-17-0462.1
- Liu, Z., Risi, C., Codron, F. e. a., He, X., Poulsen, C. J., Wei, Z., et al. (2021). Acceleration of western Arctic sea ice loss linked to the Pacific North American pattern. *Nature Communications*, 12, 1519. https://doi.org/10.1038/s41467-021-21830-z
- Lu, J., Liu, F., Leung, L. R., & Lei, H. (2020). Neutral modes of surface temperature and the optimal ocean thermal forcing for global cooling. npj Atmospheric and Climate Sciences, 3. https://doi.org/10.1038/s41612-020-0112-6
- Marshall, J., & Molteni, F. (1993). Toward a dynamical understanding of planetary-scale flow regimes. *Journal of the Atmospheric Sciences*, 50, 1792–1818. https://doi.org/10.1175/1520-0469(1993)050<1792:TADUOP>2.0.CO;2
- Nitta, T. (1987). Convective activities in the tropical western Pacific and their impact on the Northern Hemisphere summer circulation. Journal of the Meteorological Society of Japan. Ser. II, 65, 373–390. https://doi.org/10.2151/jmsj1965.65.3_373
- Ogi, M., Yamazaki, K., & Wallace, J. M. (2010). Influence of winter and summer surface wind anomalies on summer Arctic sea ice extent. Geophysical Research Letters, 37, L07701. https://doi.org/10.1029/2009GL042356
- Palmer, T. N. (1999). A nonlinear dynamical perspective on climate prediction. *Journal of Climate*, 12, 575–591. https://doi.org/10.1175/1520-0442(1999)012<0575;ANDPOC>2.0.CO:2
- Runge, J., Bathiany, S., Bollt, E., Camps-Valls, G., Coumou, D., Deyle, E., et al. (2019). Inferring causation from time series in Earth system sciences. Nature Communications, 10, 2553. https://doi.org/10.1038/s41467-019-10105-3
- Screen, J. A., & Deser, C. (2019). Pacific Ocean variability influences the time of emergence of a seasonally ice-free Arctic Ocean. *Geophysical Research Letters*, 46, 2222–2231. https://doi.org/10.1029/2018GL081393
- Seager, R., Cane, M., Henderson, N., Lee, D.-E., Abernathey, R., & Zhang, H. (2019). Strengthening tropical Pacific zonal sea surface temperature gradient consistent with rising greenhouse gases. Nature Climate Change, 9, 517–522. https://doi.org/10.1038/s41558-019-0505-x
- Stroeve, J. C., Kattsov, V., Barrett, A., Serreze, M., Pavlova, T., Holland, M., & Meier, W. N. (2012). Trends in Arctic sea ice extent from CMIP5, CMIP3 and observations. *Geophysical Research Letters*, 39, L16502. https://doi.org/10.1029/2012GL052676
- Tsuyuki, T., & Kurihara, K. (1989). Impact of convective activity in the western tropical Pacific on the East Asian summer circulation. Journal of the Meteorological Society of Japan. Ser. II, 67, 231–247. https://doi.org/10.2151/jmsj1965.67.2_231

WU ET AL. 9 of 9